https://doi.org/10.1016/j.msea.2018.04.06

Processing and Characterisation of Carbon Nanotube-Reinforced Magnesium Alloy Composite Foams by Rapid Microwave Sintering

Akeem Damilola Akinwekomi, Wing-Cheung Law, Man-Tik Choy, Ling Chen, Chak-Yin Tang*, Gary Chi-Pong Tsui, Xu-Sheng Yang

Department of Industrial and Systems Engineering, The Hong Kong Polytechnic University, Hung Hom, Kowloon, Hong Kong, China

*Corresponding author. Tel.: +852 2766 6608; fax: +852 2362 5267. E-mail address: cy.tang@polyu.edu.hk (C.-Y. Tang).

Abstract

The present study proposes an efficient processing scheme for fabricating carbon nanotubes (CNTs)-reinforced magnesium (Mg) alloy AZ61 composite foams with enhanced compressive and energy absorption properties. The scheme combines powder metallurgy, rapid microwave (MW) sintering, and pore wall reinforcement to overcome the low strength, non-uniform pore structure, prolonged sintering process, and high production cost associated with conventional unreinforced Mg-based foams. In the proposed scheme, a dual-stage mixing method is used to homogeneously disperse and incorporate CNTs into the matrix for strength enhancement, and susceptor role, and carbamide granules are used to control the pore size and porosity fractions. In addition, MW sintering is used to rapidly consolidate the samples in 20 minutes through the synergy between an external and an internal susceptor (i.e. CNTs), which facilitates uniform and volumetric heating of the entire samples. Thus, sample oxidation and the formation of deleterious secondary phases are minimised, while up to 69% energy is saved. Experimental results show that the dispersion and incorporation of CNTs into the matrix, via the present processing scheme, clearly enhance the compressive and energy absorption properties of the composite foams, as compared with the unreinforced foams. The proposed processing scheme is a rapid and energy-saving efficient technique, which can be used to fabricate high quality Mg alloy composite foams with improved compression and energy absorption properties.

Keywords Microwave sintering, Magnesium alloy, Powder metallurgy, Mechanical properties, Metallic foam

1. Introduction

Metallic foams have high specific properties and are potentially useful for energy absorption, impact resistance, damping and lightweight structural applications. The lightweight characteristic of magnesium (Mg)-based foams possesses huge potential to increase fuel efficiency and reduce emissions for automotive and aerospace applications. Nevertheless, high production costs and processing difficulties are some of the problems encountered in the fabrication of Mg-based foams [1]. Furthermore, the low strength of Mg-based foams has majorly limited them to biomedical applications. As a result, Mg-based foams have not received the same research attention unlike aluminium (Al)-based foams which have been widely studied.

The melt-foaming route is commonly utilised for producing Mg-based foams. Although this processing route can produce high porosity foams, poor control over pore size and morphology are its prominent disadvantages [2]. Moreover, the variation in pore sizes and irregular cell shape can result in anisotropic mechanical properties [3]. Furthermore, prominent foaming/gas release agents, such as calcium hydride and titanium hydride, are expensive [4], while alternative agents, such as calcium carbonate ($CaCO_3$), release poisonous gases during decomposition at the foaming temperature [5]. Therefore, there is a need to find alternative solutions that are simple, cost effective and capable of producing high quality Mg foams.

The powder metallurgy (PM) processing technique is a relatively simple fabrication process that offers near-net shape production and can accommodate the incorporation of relatively high reinforcement fractions for fabricating metal matrix composites (MMCs) [6]. This technique has been successfully utilised to control the pore shape and size of a steel composite foam by using steel hollow spheres as spacing holding agents [7]. Similarly, some studies have shown that steel foams fabricated with spherical space holders possess higher compressive properties than foams having irregular pores [8]. Therefore, the PM technique can overcome some of the challenges encountered with using the melt processing technique.

Nonetheless, the consolidation of PM products is typically done through conventional sintering, which generally requires a prolonged sintering time of several hours. This increases the cost of production and the propensity for the formation of undesirable secondary phases. For instance, Mg foams were sintered for up to 48 hours, which resulted in excessive grain growth, reduced porosity, and deleterious reactions between the base material and the silicon crucibles [9]. Other similar studies on Mg foams that required less sintering time in the range of 2 hours [10] and 6 hours [2] have reported a partial oxidation of the matrix. With the aim of harnessing the advantages of the PM processing technique for the fabrication of Mg foams, alternative rapid sintering methods, such as microwave (MW) sintering, have been developed. Successful MW sintering and improvement in the mechanical properties of AZ61 Mg composites [11] and biomedical properties of titanium composites [12] have been reported. Compared with conventional sintering, the advantages of MW sintering include rapid heating rates, volumetric heating, reduced sintering time and energy consumption [11,12].

Carbon nanotubes (CNTs) have low density, high strength, high elastic modulus, and high aspect ratio, which make them ideal reinforcement materials for both polymer [13–15] and metal matrices [11,16,17]. An improvement of 25 to 40% in the yield strengths of Mg-based composites reinforced with 1 vol.% CNTs has been reported [16]. Similarly, Duarte et al. [17] report an increment of 100% in the Vickers microhardness of Al-foams reinforced with CNTs. Notwithstanding the property improvement reported in the above studies, achieving a homogenous dispersion of CNTs in the matrix and maintaining their structural integrity are some of the challenges encountered in the processing of CNT-reinforced MMCs [18]. Therefore, some fabrication techniques including ultrasonication processing [19] and mechanical milling [18] have been reported. Mechanical milling [20,21] has emerged as a good dispersion method, by which the structural integrity of the CNTs can be retained when the processing parameters are optimised [22]. In addition to the reinforcement effect of CNTs in the matrix, they could also serve as MW susceptors for enhancing volumetric heating, accelerating the heating rate, and reducing the overall sintering time [23].

Many previous studies on Mg-based foams have targeted orthopaedic implant applications, where relatively low strengths comparable to those of bone tissues are required [24,25]. Mg-based

foams, with higher compressive strength and energy absorption capability, are required for high performance automobile or aerospace applications. A promising approach to address the low strength of Mg-based foams is to reinforce the Mg matrix with high strength particles, such as CNTs. As a result, the application areas of Mg-based foams could be broadened to different industries, such as automobile and aircraft. However, the synthesis of CNT-reinforced Mg-based composite foams by means of MW sintering has not been reported.

Therefore, this study proposes an efficient processing scheme, comprising powder metallurgy, rapid microwave sintering, and matrix reinforcement for the fabrication of Mg alloy AZ61 composite foams to improve their compressive and energy absorption properties. In the proposed scheme, spherical carbamide granules are used to simultaneously control the pore shape, size and porosity of the specimens. CNTs are selected to perform a dual function, serving as matrix reinforcement material and as an internal susceptor, for accomplishing volumetric heating. The MW sintering process is enhanced by the synergy between the internal and external heating, which results in rapid sintering, minimises the formation of unwanted secondary phases, and reduces the overall sintering time for cost and energy savings. The effect of CNTs on the compression and energy absorption behaviour of the foams are also investigated. The results reported in this study can provide useful knowledge in the design of lightweight structural materials using MW technology.

2. Experimental procedures

2.1 Materials

The materials used in this study include water atomised Mg AZ61 alloy powder (150 – 300 μm, Tangshan Weihao Powder Co., Ltd, China), multiwalled carbon nanotubes (CNTs, purity >95 wt.%; internal diameter: 3 – 5 nm; outer diameter: 8–15 nm; length: ~50 μm; Chinese Academy of Sciences, Chengdu Organic Chemistry Co., Ltd., China), commercially available spherical carbamide granules (0.2 – 0.9 mm) and Zwitterionic surfactant, 3-(N,N-dimethyl stearyl ammonio) propanesulfonate, (TCI (Shanghai) Chemicals, Development Co., Ltd, China). Mechanical milling was used to reduce the particle size of AZ61 to ~ 50 μm to enhance its MW absorbability. Details of the milling process have been reported in a previous work by [11].

2.2 Synthesis of CNT-reinforced AZ61 composite foams

The CNTs used in this work are expected to perform a dual role, i.e., as matrix reinforcement and MW absorption, which can contribute to accelerating the sintering process [11]. CNTs were first purified and functionalised by refluxing in a 3:1 mixture of 98% sulphuric acid and 68% nitric acid. The dispersion procedure was as follows: 1 g of the surfactant powder was dissolved in 150 mL of ethanol and ultrasonicated at 27 °C for 15 minutes. After the complete dissolution of the surfactant powder in ethanol, 3 g of CNTs were added to the mixture, which was further subjected to ultrasonication for 20 minutes for the complete dispersion of CNTs in the solution. Stoichiometrically calculated amounts of AZ61 powder were added to the ethanol-CNTs-surfactant mixture, to make 1, 2, 3 and 5 % volume fractions (vol.%) of CNTs. The resulting composite mixture was designated as AZ61/*x*% CNTs, where *x* is the volume fraction of CNTs in the mixture. The AZ61/CNTs slurry was sonicated at 60 °C to disperse the CNTs on the alloy powder and to evaporate the ethanol. The composite paste was collected and dried under vacuum at 80 °C for 8 hours. After drying, the composite powder was put in a milling jar with equal weight proportion of two different sizes of hardened stainless-steel balls (Ø 8 mm and Ø 15 mm) and milled at 300 rpm for 60 minutes. The ball-to-powder charge ratio was 10:1 and 30 vol.% of cyclohexane was added as a process control agent to minimise cold welding and to increase powder yield. To assess the structural integrity of the CNTs after the mechanical milling treatment, Raman spectra were collected under ambient conditions using a microspectrometer (Horiba Jobin Yvon, HR800), utilising a visible red excitation laser source of 632.8 nm and a power of 50 mW.

With the CNTs dispersed on the surface of the AZ61 alloy powder, carbamide granules were added to the composite powder and further mechanically mixed for 10 minutes. About 2 mL of ethanol was added to moisten the surface of the carbamide granules and to minimise particle segregation during mixing. The AZ61/CNTs/carbamide mixture was put in a rigid cylindrical die and uniaxially pressed at 350 MPa for 2 minutes to form green samples. The green samples were immersed in room temperature DI water for 3 hours to eliminate the carbamide granules and subsequently generate the pore structure. Porous green samples were dried at 150 °C for 5 hours prior to MW sintering.

2.3 Microwave sintering of foam samples and X-ray diffraction (XRD) analyses

The MW furnace used for sintering was a continuously adjustable 3 kW multimode high vacuum cavity operating at 2.45 GHz (HAMiLab-HV3; SYNOTHERM Corporation). MW power for the sintering operation was varied between 100 and 350 W to maintain a steady sintering temperature. A susceptor-enhanced MW sintering setup was used to rapidly sinter the samples at 500 °C for 20 minutes under a flowing high purity argon gas to minimise sample oxidation. The green samples were enclosed in a cylindrical susceptor kiln lined with a mixture of silicon carbide and graphite (SiC/graphite). X-ray diffraction studies were carried out to identify the phases present in the AZ61 powder and the sintered foam samples using a Rigaku SmartLab 9 kW XRD equipment. The samples were exposed to Cu Kα radiation (λ = 1.54056 Å) at a scanning speed of 4°/ min.

2.4 Microstructural, density, and X-ray micro-computed tomography

A field emission scanning electron microscope (FESEM, JEOL JSM-6335F) was used to evaluate and visualise the dispersion of CNTs on the alloy powder after the surfactant treatment and mechanical milling operations. The sintered density and porosity of the foam samples were determined from the analyses of the images obtained from X-ray micro-computed tomography (micro-CT, Skyscan1076) scans, using the average value of at least three samples from each set. Other morphological characteristics, including pore size, shape, and total porosity were also derived from the micro-CT data. The source voltage and current were 88 kV and 100 µA, respectively. The image pixel size was 17.33 µm. The AZ61 matrix appeared as light grey while the pores were black in the images, which were processed and analysed using the instrument's software (CT Analyser).

2.5 Compression test

Uniaxial compression tests were performed on cylindrical samples with a height-to-diameter ratio of 1.5 on an MTS810 universal testing machine at ambient temperature. The machine's cross-head speed was 1 mm/min. A minimum of five specimens were tested in each set to get an average result and to assess the repeatability of the experimental procedure and the results obtained. The compressive strengths of the foams were determined from the stress (σ)–strain (ε) curve, while

their energy absorption capacities (E) were evaluated from the surface area under stress-strain curve up to 40% strain, using the expression in Eq. 1:

$$E = \int_0^{\varepsilon} \sigma \, d\varepsilon \qquad (1)$$

3. Results

3.1 Synthesis of CNT-reinforced AZ61 composite foams and Raman spectroscopy

CNTs are successfully dispersed and incorporated into the AZ61 alloy matrix using the combined surfactant and mechanical milling approaches. In Fig. 1a, the as-received CNTs appear as a bunch of entangled wires. After treating them with the surfactant and ultrasonication, CNT wires (white arrows in Fig. 1b) are shown to be well dispersed on the surface of the alloy powder, indicating that the surfactant dispersal technique is quite effective and up to 3 vol.% CNTs are successfully dispersed. Mechanical milling, for 30 minutes (Fig. 1c) and 60 minutes (Fig. 1d), is further utilised to impinge the CNTs (white arrows) to the surface of AZ61. An attempt to increase the volume fraction of CNTs to 5 vol.% in the composite mixture is not successful, as agglomerates of CNTs remain on the alloy powder (dashed circle in Fig. 1e). Further mechanical milling of the composite mixture for 60 minutes does not significantly improve the dispersion of the CNTs and some agglomerates (dashed circles) can still be seen in Fig. 1f. Therefore, further processing and characterisation of the samples are limited to 3 vol.% CNT-reinforced samples.

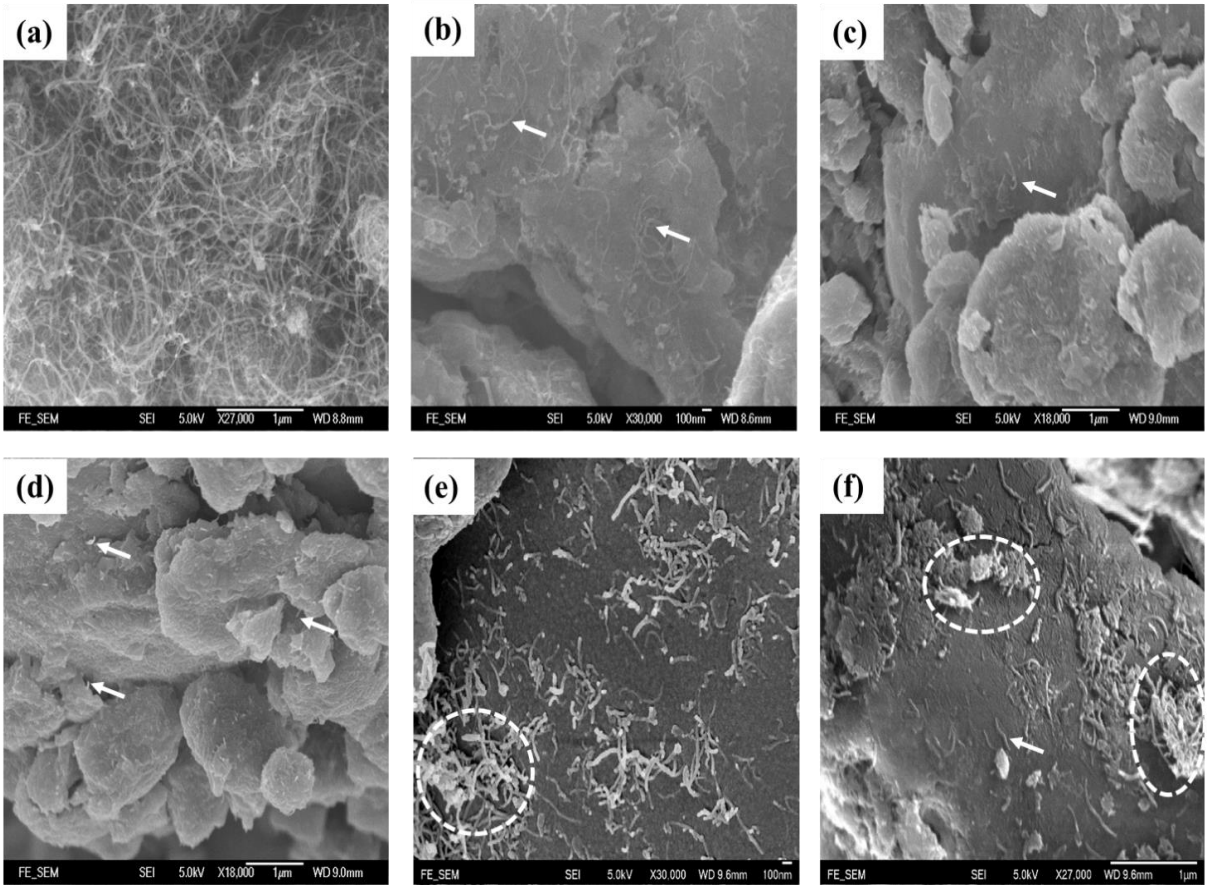

Fig. 1. FESEM micrographs of (a) entangled mass of as-received CNTs; (b) homogeneous distribution of CNTs on AZ61 powder after surfactant treatment (AZ61/3vol% CNT); (c) CNTs embedded on AZ61 surface after milling for 30 minutes (AZ61/3vol% CNT) (d) after milling for 60 minutes (AZ61/3vol% CNT); (e) agglomerates of CNTs in AZ61/5vol% CNT; and (f) persistent agglomerates of CNTs after milling (e) for 60 minutes

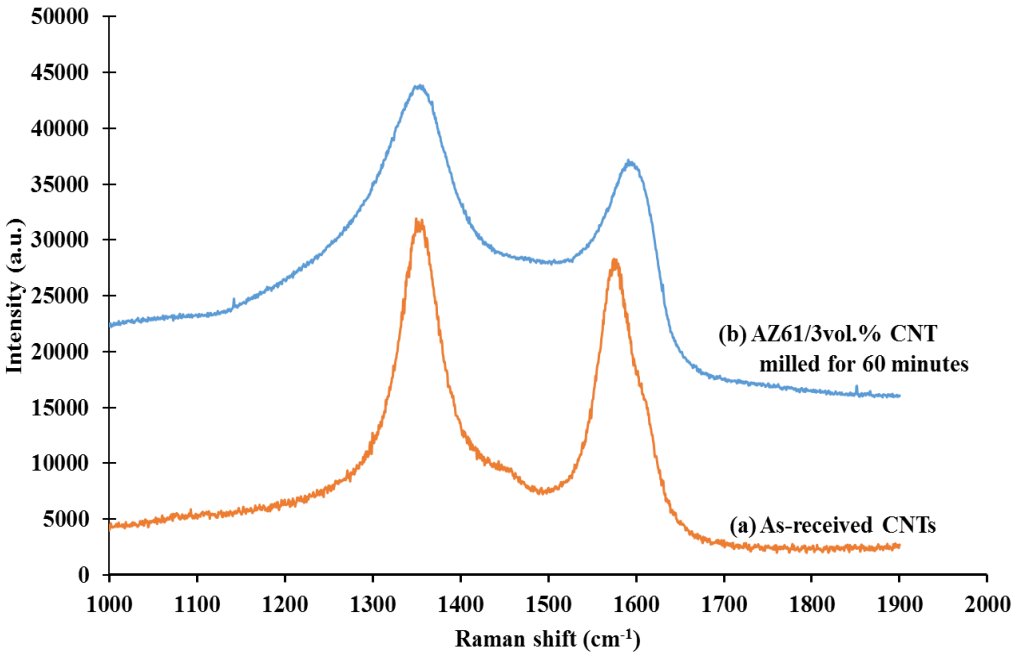

Fig. 2. Raman spectra of (a) as-received CNTs and (b) AZ61/3vol% CNT milled for 60 minutes

Raman spectra of AZ61/CNTs mixture are measured after 60 minutes of mechanical milling to assess the structural integrity of the CNTs. From the results, as shown in Fig. 2, the two peaks that appear at ~ 1352 and 1577 cm^{-1}, represent the D (defect) and graphitic G-lines, respectively. An increase in the relative intensities of the two peaks (I_D/I_G) is a qualitative indication of CNTs damage during processing [22]. A comparison of the results of the I_D/I_G ratio presented in Table 1, indicates that there is no significant difference between those of as-received CNTs and milled CNTs. Therefore, it may be concluded that CNTs are not structurally compromised during the milling process used in this study.

Table 1 Raman spectra of as-received CNTs and AZ61/3% CNTs milled for 60 minutes

Milling time (min)	0	60
I_D/I_G ratio	**1.1532**	**1.1742**

3.2 Microwave sintering of composite foams and XRD analysis

PM and rapid MW sintering techniques are successfully used to synthesise CNT-reinforced Mg AZ61 alloy composites. The SiC/graphite-lined kiln serves as an external susceptor to initially heat the samples externally until they couple and absorb the MWs. The CNTs incorporated into the matrix are good MW absorbers and act as internal susceptors to initiate volumetric heating. It can, therefore, be stated that the synergy between these susceptors i.e. CNTs/SiC/graphite leads to a rapid temperature rise in the samples, suppresses the formation of secondary unwanted phases, and reduces the total sintering time to about 20 minutes.

XRD patterns of milled AZ61 powder and sintered foam samples with 49% porosity are shown in Fig. 3. Although the matrix is filled with CNTs, no carbon peaks are detected in the diffractograms. A plausible explanation for this observation could be due to the limit of X-rays in detecting signals from components with low concentrations [26]. Apart from the prominent peaks of Mg found in all the samples, two weak peaks appear at 2θ = 36.05° and 40.05°, which are indexed as the intermetallic compound $Al_{12}Mg_{17}$. These peaks have been identified in all composite samples as well as in the as-received AZ61 powder, indicating that $Al_{12}Mg_{17}$ is not precipitated during MW sintering. It is very likely to have been formed during the production process of the alloy powder. Furthermore, MgO peak is not detected in the X-ray patterns of the sintered samples due to the rapid heating rate in the MW sintering process. These results further show the advantages of MW sintering over other conventional sintering techniques.

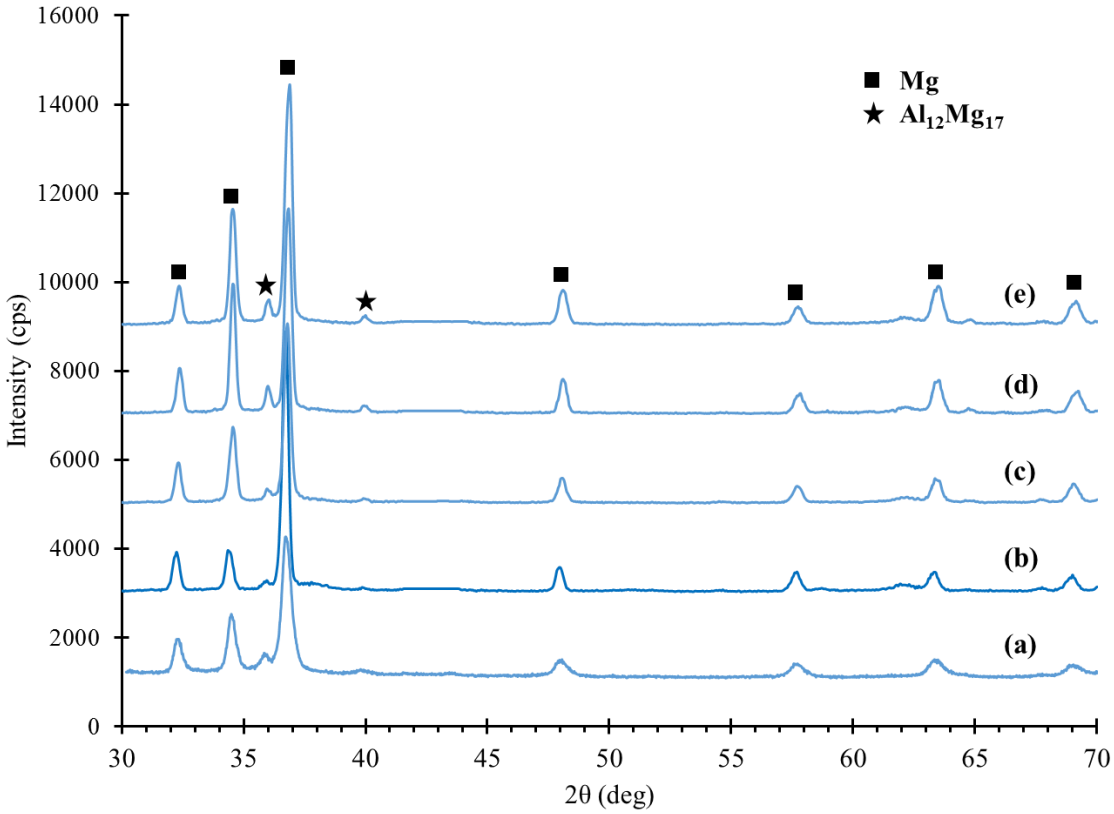

Fig. 3. XRD patterns of (a) AZ61 powder, (b) sintered AZ61 foam, (c) sintered AZ61/1vol% CNT foam (d) sintered AZ61/2vol% CNT foam and (e) AZ61/3vol% CNT foam. Foam porosity is 49%.

3.3 Density, porosity, and microstructural characterisations

Density and porosity data of the sintered specimens are shown in Table 2. Generally, CNT-reinforced foam samples exhibit a slightly higher density in contrast to the unreinforced foam matrix. As CNTs have a higher density of 2.6 g/cm^3 in comparison with 1.8 g/cm^3 for the AZ61 matrix, the experimental density of the CNT-reinforced composite foams slightly increases as the volume fraction of CNTs is increased. Internal microstructures of the foam samples, obtained from micro-CT scans, are shown in Fig.4. The pores are spherical and evenly distributed in the matrix, with pore sizes varying from 0.2 to 0.9 mm. Porosity in the two sets of samples is ~ 49% and 62%. The spherical shape of the pores is retained after the sintering process, which suggests

that the compaction pressure utilised for making the green samples preserves the shape of the pores. Control over pore morphology is one of the advantages of using the PM-based space holder technique for the fabrication of foam samples. By the appropriate selection of the size and shape of the space holding agent, the pore size, shape, and its distribution can be controlled [7,8], which is barely attainable using melt-based foaming techniques.

Table 2 Comparison of the porosity, density, pore diameter and compressive characteristics of porous AZ61/CNTs composite foams and metallic foams

Matrix material	Porosity (%)	Density ($g \cdot cm^{-3}$)	Pore diameter (mm)	Compressive strength (MPa)	Energy absorption[b] ($MJ \cdot m^{-3}$)	Reference
AZ61	49	0.92	0.2-0.9	24.49±1.33	6.45±0.90	This work
AZ61/1% CNTs	48	0.94	0.2-0.9	35.91±0.92	9.78±0.28	This work
AZ61/2% CNTs	48	0.94	0.2-0.9	40.19±2.17	11.69±0.99	This work
AZ61/3% CNTs	49	0.92	0.2-0.9	47.24±3.91	16.18±1.60	This work
AZ61	62	0.68	0.2-0.9	15.77±1.96	7.19±0.42	This work
AZ61/1% CNTs	62	0.69	0.2-0.9	24.66±1.08	7.98±0.54	This work
AZ61/2% CNTs	63	0.67	0.2-0.9	27.15±1.91	9.99±1.53	This work
AZ61/3% CNTs	62	0.69	0.2-0.9	30.38±0.98	12.35±1.45	This work
AZ91	52	0.86	0.75	18	5.41	[25]
Mg	53	0.82	2.00	27.80	7.75[a]	[27]
Mg	53	0.83	1.25	14.60	3.66[a]	[28]
Mg	55	0.78	0.25	12.30	1.12[a]	[24]
Mg-(3-5%)SiC	65-70	0.57	1-1.5	7.5	1.96[a]	[29]
AZ91	66	0.60	0.75	10	2.36	[25]
$AlSi_9Mg$	69	2.07	-	7	2.27	[30]
$AlSi_9Mg$-5%SiC	69	2.08	-	10	3.71	[30]
$AlSi_9Mg$-5%SiC	58	1.75	-	20	7.47	[30]

NB: **a**: estimated value; **b**: estimated at 40% strain

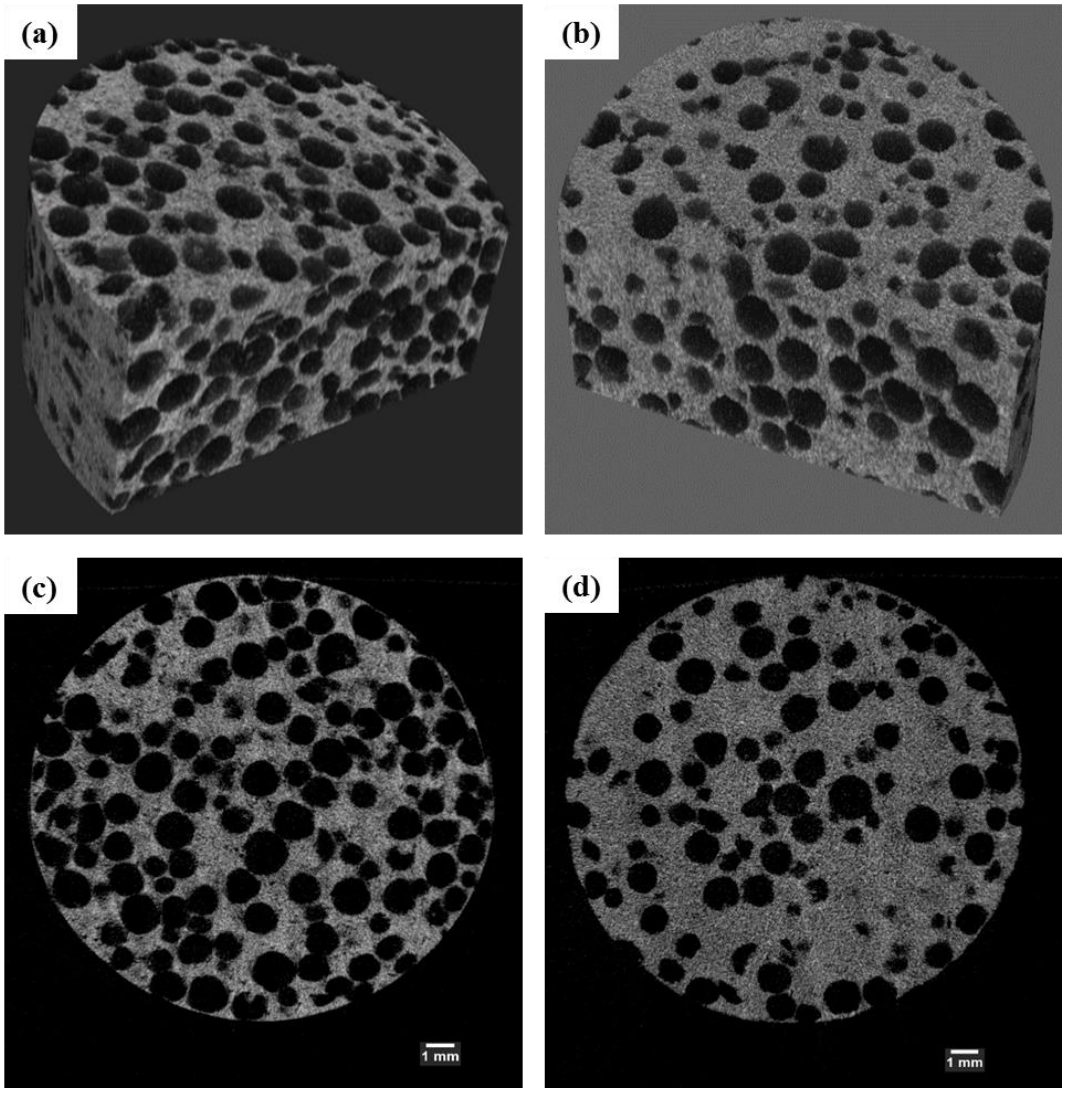

Fig. 4. Reconstructed 3D micro-CT images of AZ61 foams (a) 62% porosity (b) 49% porosity and longitudinal 2D slices through the foam samples (c) 62% porosity (d) 49% porosity.

3.4 Compression test results

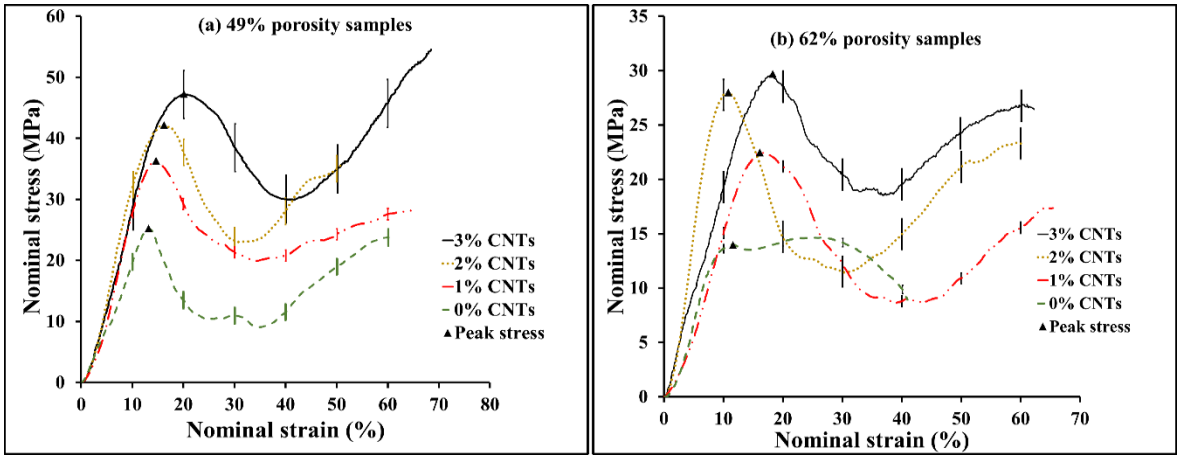

Fig. 5. Nominal compressive stress-strain curves of samples with (a) 48% porosity and (b) 62% porosity

The nominal uniaxial compressive stress-strain curves of the foam samples presented in Fig. 5 are typically characteristic of metallic foams, as reported in some previous studies [25,27]. The error bars are the standard deviation values of stress values at intervals of 10% strain. All the curves show an initial linear elastic section ending at a peak stress, a decline in the peak stress up to a relatively stable stress level (plateau section), and a densification section, where the nominal stress increases. Values of the compressive strength and energy absorption capacity of the samples and some previous works are summarised in Table 2.

The compressive strength is defined as the peak stress (denoted by a solid triangular marker), which terminates the linear elastic section observed in Fig. 5. The energy absorption capacity is calculated based on the expression given in Eq.1. As porosity increases in the samples, their compressive strength and energy absorption ability decrease, regardless of the presence of CNTs. However, with increasing volume fraction of CNTs in the matrix, the compressive strength and energy absorption properties are significantly improved.

4. Discussions

4.1 Synthesis of CNT-reinforced AZ61 composite foams and Raman spectroscopy

The surfactant utilised in this study for dispersing CNTs belongs to the linear-type zwitterionic category, which has both hydrophobic and hydrophilic head groups [16]. These groups attach to clusters of CNTs and because of a strong dipole/dipole electrostatic attraction that exists between the negative tail of the surfactant and a CNT, bundled CNTs are isolated into individual strands as shown by the white arrows in Fig. 1b. A similar dispersion result has been reported for a Mg/1 wt.% CNTs composite mixture [16]. However, a higher loading fraction of CNTs (3 vol.%, equivalent to 3.5 wt.%) is utilized in this study and a good dispersion of CNTs on the AZ61 powder has been achieved. This can be attributed to the beneficial effect of the ultrasonication step. Moreover, the volume fraction of CNTs dispersed in this study supersedes the maximum 0.75 wt.% of CNTs dispersed on Al powder using only the ultrasonication method in the study reported in Ref. [19]. The results from the present study suggest that the surfactant technique combined with ultrasonication is an effective method for dispersing CNTs during the fabrication of MMCs.

Low energy mechanical milling is found to be effective in further achieving uniform CNTs-dispersal, breaking-up agglomerates of CNTs, and embedding them within the matrix of the alloy powder, to serve as internal susceptors during the MW sintering stage. In an earlier study [31], the authors utilise mechanical milling for dispersing and embedding CNTs in aluminium (Al) powder, which requires a duration of six hours. However, severe agglomeration, due to the excessive cold welding of Al particles, occurs at the same time. In this present study, the milling parameters are carefully designed and adjusted so that a significantly shorter milling time (~1 hour) for incorporating the CNTs into AZ61 particles could be achieved.

CNTs are excellent absorbers of microwaves and can be heated up rapidly [23]. Therefore, volumetric heating can be achieved, which can drastically reduce the overall sintering time from the several hours in conventional sintering to a few minutes in MW sintering. An attempt to increase the volume fraction of CNTs to 5 vol.% in the composite mixture was not successful, as agglomerates of CNTs remained on the alloy powder (dashed circle in Fig. 1e). Further

mechanical milling of the composite mixture for 60 minutes did not fully disperse the CNTs and some CNTs agglomerates could still be observed (Fig. 1f).

From the results presented in Table 1, there is no significant difference between the I_D/I_G ratios of as-received CNTs and milled CNTs. This indicates that the milling conditions do not cause damage to the CNTs. Moreover, AZ61 powder particles may act as shock absorbers and reduce the impact of the milling balls on CNT [11]. This shielding effect is expected to be multiplied once CNTs are embedded within the particles. Some earlier studies have shown that inappropriate milling conditions, such as excessively prolonged milling time [32] and very low milling intensity that exposes CNTs to direct collision with the milling balls [33], may significantly damage the CNTs, thus affecting the strength of the resulting composites.

4.2 Microwave sintering of composite foams and X-ray diffraction study

Prior studies on the conventional sintering of Mg-based foams have reported sintering times of 2 hours [10], 6 hours [2] and even up to 48 hours [9]. The results from those studies have indicated that a prolonged sintering time can result in the oxidation of the matrix, the formation of undesirable secondary phases, and the reduction of number of pores. Magnesium oxide (MgO) is commonly found as the secondary phase, and can adversely affect the mechanical properties of the samples as confirmed in the study reported in Ref. [16].

A prolonged sintering time increases energy consumption and production cost. In this study, rapid MW sintering has been used to consolidate AZ61/CNTs foams in 20 minutes, using a SiC/graphite lined kiln for external heating and CNTs for enhancing volumetric heating in the samples. This results in a high heating rate, minimises matrix oxidation, and suppresses the formation of secondary MgO phase, as shown in the XRD diffractogram in Fig.3. In comparison with the studies reported in Refs. [10] and [9], the sintering time in this study is significantly reduced by 87.5% and 99.5%, respectively. A shortened sintering cycle is beneficial in reducing the energy consumption and production cost, as well as eliminating the intermittent holding times required for homogenisation in conventional sintering.

Sankaranarayanan et al. [34] have reported a lower MW sintering time of 17 minutes at 900 W during the processing of a Mg syntactic foam containing fly ash hollow spheres. However, in this

study a lower MW power range that is utilised implies that a significantly lower energy is consumed for fabricating the composite foams, as highlighted in Table 3.

Table 3 Estimation of energy saving in microwave sintering of magnesium-based composite foams.

Matrix	MW Sintering power (kW)	Time (hours)	Energy consumed kWh	Energy saved* (%)	Reference
Mg	0.90	0.28	0.26	-	[34]
AZ61	0.23	0.33	0.08	69	Present work

** estimated with reference to the data in Ref.* [34]

The MW sintering power utilised in this work varies between 100 and 350 W. By taking an average of this range and considering the total sintering time, energy consumption is estimated to be about 0.08 kWh, which represents a remarkable 69% reduction in energy consumption.

4.3 Density, porosity, and microstructural characterisations

The microstructures presented in Fig. 4 show that the pores are not distorted. Distortion of pore shape due to excessive compaction pressure have been reported in some studies [10,35]. Furthermore, excessive compressive pressures can hermetically seal spacer materials in the matrix and lead to contamination [24] and prolonged or incomplete leaching [36]. Foams processed in the liquid state by gas blowing/releasing agents typically exhibit irregular pore shapes and wide pore size distribution [27,29], which have been implicated in inducing anisotropy in the mechanical properties of some foams [3]. In the present study, carbamide granules are used to control the pore shape and distribution of pores.

The pore morphology in samples with 62% porosity (Fig. 4a and c) show interconnectivity due to the higher volume fraction of carbamide used for generating the pores. A high-volume fraction of the space holder agent can give rise to a high porosity, enable intercommunication between adjacent cells and result in open-cell foams. Such open pore foams, with interconnecting cell

structures, can be useful in damping and sound absorption applications [36]. Conversely, samples with 49% porosity, as shown in Fig. 4b and d, have been fabricated with a lower volume fraction of spacer materials. Hence, their pore morphology reveals isolated closed-pores with very minimal interconnectivity, which have potential applications in energy absorption [37].

4.4 Compression test results

The summary of the compression tests and energy absorption characteristics of the samples presented in Table 2 indicates that these properties have been enhanced by CNTs. Only a few studies have been reported on CNT-reinforced metallic foams. Improvement in the compressive and energy absorption properties of melt-processed Al-CNTs composite foams up to 0.8% CNT content is reported in Ref. [38]. However, the compressive strength of 1% CNT foam is slightly lower than that of the unreinforced matrix. In another study [17], the Vickers microhardness of CNT-reinforced Al-alloy composite foams is found to be about 56% higher than the unreinforced foams.

In the present study, significant improvement in both compressive and energy absorption properties have been observed in CNT-reinforced Mg composite foams. For samples with 3% CNTs fraction and 49% porosity level, improvements in compressive strength and energy absorption are ~93% and 153%, respectively, as compared with the unreinforced foam sample. Similar improvement trends are also observed in foam samples with 62% porosity levels. These results show that CNTs clearly enhance the compressive and energy absorption properties of the foams.

Referring to Fig. 5, the apparent elastic moduli are similar in the graph plot of 49% porosity samples. However, in the graph plot of 62% porosity samples, it shows that the incorporation of CNTs may affect the apparent elastic moduli. The 2% CNTs-contained sample shows the largest quasi-elastic modulus from the start to the first maximum compressive strength. A reduction in the apparent elastic modulus can be seen as the volume fraction of CNT increased from 2% to 3%. It is anticipated that the addition of CNTs can initially stiffen the porous structure of the sample. When the volume fraction of CNT further increases, stress concentration causing

localised premature yielding at the filler-matrix interface will be more intense, and therefore, the apparent elastic modulus is then reduced. This effect is expected to be apparent for the 62% porosity samples with opened cell morphology.

The compressive strengths of all the samples are also higher than the 7.5 MPa reported for Mg foam reinforced with SiC particles [29]. Bulk Mg has limited ductility due to its hexagonal closed-pack crystal structure, which restricts the number of slip systems that are available for deformation [26]. The presence of ceramic reinforcement particles can aggravate its brittleness as shown by the results in Ref. [29]. Furthermore, the compressive strengths and energy absorption properties reported in the current work compare favourably with some Al foams [30] reinforced with SiC particles, as presented in Table 2.

The enhancement in the compressive strength of the composite foams in comparison with the unreinforced matrix can be rationalised in two ways; due to the presence of CNTs and the spherical shape of the pores. By considering the latter reason, strengthening mechanisms such as elastic modulus (EM) mismatch between the matrix and the reinforcing particles and stresses arising from the differential thermal expansion between the matrix and the reinforcement, have been proposed to be responsible for the improvement in the yield strengths of nano-particle reinforced metal matrix composites [6,26].

Regarding the second argument on the morphology of the pores, spherical carbamide granules are chosen over angular ones to minimise stress concentrations at the corners of the pores during loading. This proposition is supported by some studies on Al foams [3] and steel foams [8], in which both angular and irregular pore shapes have been reported to decrease the mechanical properties of such foams. Despite the significant reduction in the sintering time reported in this work, the compressive and energy absorption properties of the samples have not been compromised. In fact, they are superior to some of those earlier reported (Table 2) for similar studies on Mg-based foams and Al-based foams. This further highlights the advantages of the proposed processing technique utilised in this study.

Shima and Oyane [39] proposed some constitutive equations for predicting the yield stresses of some sintered porous pure metals by considering the influence of work-hardening and

deformation mode. The relevant equations are reproduced below and are used to investigate their suitability for modelling the compressive yield strengths of the AZ61 foam specimens.

$$f = \frac{1}{2.49}\left((1-\rho)\right)^{0.514} \qquad (2)$$

where ρ is the relative density and f describes the degree of influence of the hydrostatic stress component, σ_m on the onset of yielding of porous bodies.

Another useful function that describes the ratio of the apparent stress applied to the porous bodies and the effective stress applied to the matrix is f'. Similar to f, f' is also dependent on the relative density and it is expressed as:

$$f' = (\rho)^n \qquad (3)$$

where n is a fitting parameter that relates the yield stress of the porous body, σ_1 to its relative density. Eq. 2 and 3 can be combined and related to the yield stress of the matrix (σ_0) as follows:

$$|\sigma_1| = \frac{f'\sigma_0}{(1+1/9f^2)^{0.5}} \qquad (4)$$

Thus, by combining Eq. 2, 3, and 4, the yield stresses of porous bodies with various densities can be calculated. Some calculated results, using the experimental yield stress of the matrix σ_o and three different values of *n*, are listed in Table 4. A graph comparing the values of the experimental yield stresses and calculated yield stresses against density is shown in Fig. 6. The error bars are standard deviation values.

Table 4 Comparison of experimental with calculated yield stresses

Matrix composition	Density (g/cm3)	Relative density, ρ	Experimental yield stress, $\boldsymbol{\sigma_0}$	Calculated yield stress, $\boldsymbol{\sigma_1}$ (n = 2.0)	Calculated yield stress, $\boldsymbol{\sigma_1}$ (n = 2.5)	Calculated yield stress, $\boldsymbol{\sigma_1}$ (n = 3.0)	Reference
AZ61/2% CNT	0.67	0.372	27.15	22.85	13.87	8.50	This work
AZ61/0% CNTs	0.68	0.378	15.77	23.54	14.39	8.89	This work
AZ61/1% CNTs	0.69	0.383	24.66	24.23	14.93	9.29	This work
AZ61/3% CNTs	0.69	0.383	30.38	24.23	14.93	9.29	This work
AZ61/2% CNTs	0.94	0.522	40.19	44.98	32.38	23.49	This work
AZ61/1% CNTs	0.94	0.522	35.91	44.98	32.38	23.49	This work
AZ61/0% CNTs	0.92	0.511	24.49	43.08	30.68	22.02	This work
AZ61/3%CNTs	0.92	0.511	47.24	43.08	30.68	22.02	This work
AZ61/0% CNTs	1.69	0.939	135.50	145.38	140.86	136.49	[11]

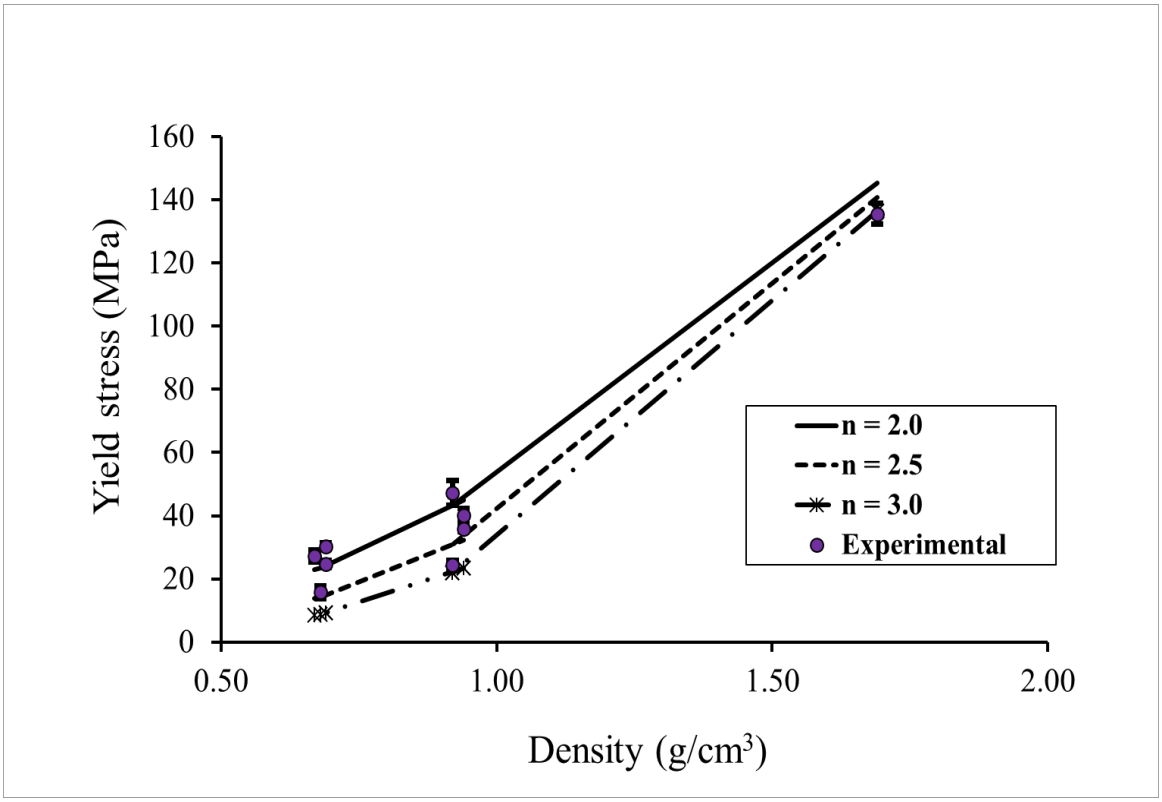

Fig. 6 Variation of yield stress with density for sintered AZ61 samples.

It can be seen from Fig. 6 that the calculated results fit quite well with the experimental findings for n = 2.0 to 3.0. In this case, higher values of n imply lower values of the yield stress $\boldsymbol{\sigma_1}$, and the equations can give reasonable estimates for both the unfilled and CNT-filled composites. Compared with the results of Shima and Oyane [39], n was set to a similar value of 2.5 for describing the yield stresses of sintered pure copper with various densities.

4.5 Deformation and failure analyses

All the samples exhibited similar stress-strain curves as presented in Fig. 5. That of a 49% porosity sample is reproduced in Fig. 7a, as a representative sample, and three distinct sections have been identified and labelled as (i) a linear elastic section, (ii) a relatively constant stress level section (plateau), and (iii) a densification section. Five different stages of the failure of a representative sample undergoing uniaxial compression are imaged and shown in Fig. 7b to f. The corresponding locations on the stress-strain curve are also identified in the plot shown in Fig. 7a. The specimen, with clear spherical pores, at the beginning of the test is shown in Fig. 7b.

As the test progresses in the linear elastic section, no significant changes are detected in the morphology of the surface pores. This linear elastic behaviour continues until the peak stress is attained. Beyond this section, a stress drop is observed. Such drop can be attributed to the initiation of cracks and the onset of collapse of the pore walls of the samples [29]. Crack initiation can arise due to several reasons, such as localized stress concentrations attributable to the clustering of pores (e.g. see Fig. 7c) or weak pore walls. Cracks that are approximately positioned parallel to the loading direction can be seen in Fig. 7c and d.

With a further increase of the applied stress, the crack elongates and propagates into the matrix, as indicated by the region enclosed within the white dotted oval shape in Fig. 7d. At this stage, the relatively horizontal part of the curve in section (ii) is associated with progressive pore fracture and collapse at an almost constant load due to buckling [29], and this stage marks the onset of densification of the foam sample. More cracks (see the region enclosed by the white dotted oval in Fig. 7e) have now appeared on the specimen as its pores collapse and are densified. The densification section (section (iii) of the stress-strain curve in Fig. 7a) is described by the total or near-total collapse and subsequent compaction of adjacent pore walls against one another.

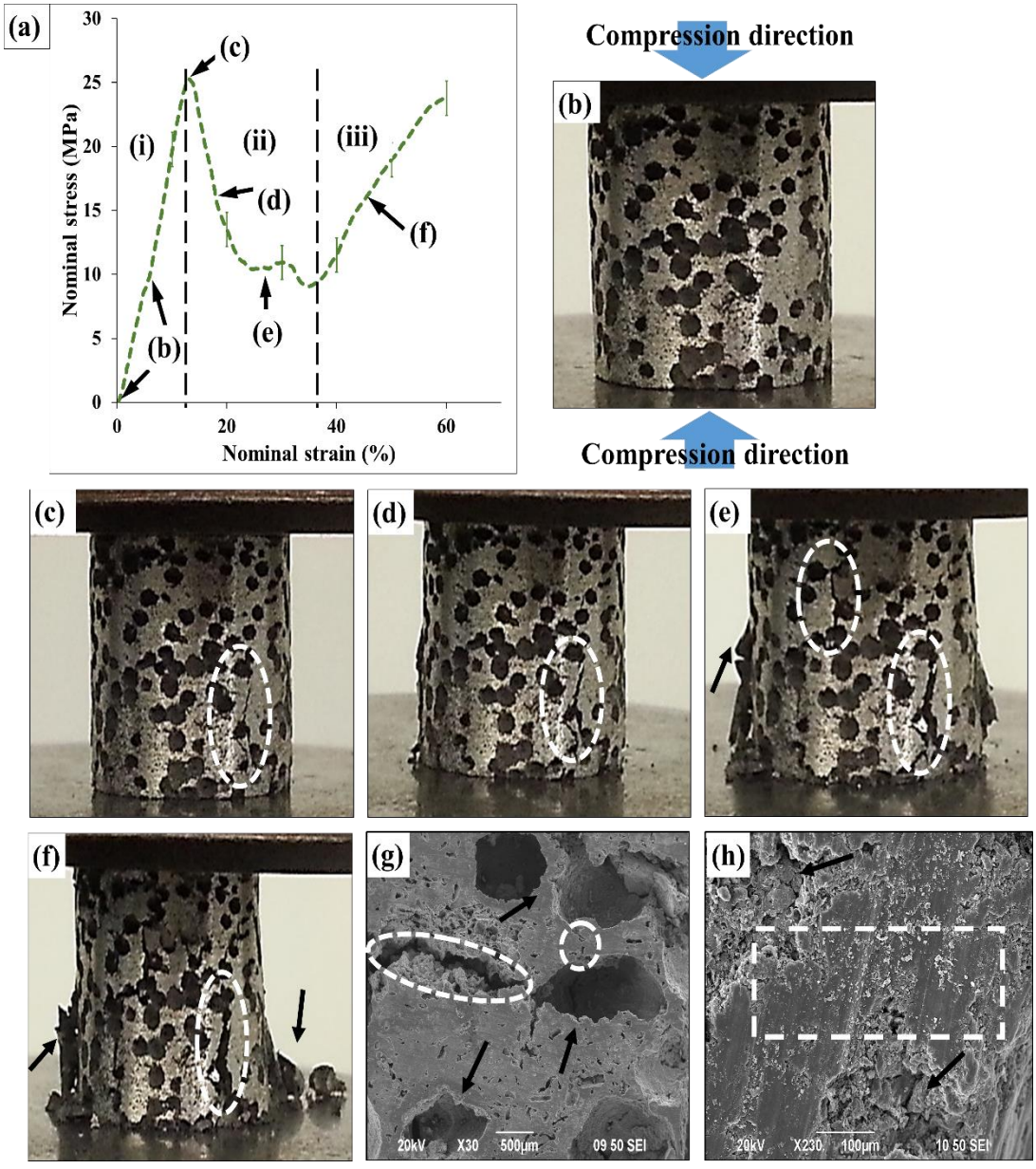

Fig. 7. (a) Typical nominal compressive stress-strain curve of a representative foam sample with 49% porosity; (b) to (f) Images of the different stages of failure of the sample under uniaxial compression as indicated by the arrows in (a); (g) SEM image of the internal microstructure of a failed surface sectioned parallel to the loading direction; and (h) SEM image of the shear bands on a failed surface.

This leads to an increase in stress, as the foam material now behaves like a dense material. Some fragments are sheared from the specimen and can be seen indicated by the black arrows in Fig. 7f.

The failed surface of the sample is further examined using a scanning electron microscope (SEM) and the images are shown in Fig. 7g and h. In Fig. 7g, the specimen is sectioned along the direction of compression using electrical discharge machining to examine the internal microstructure. It shows that several pores (black arrows in Fig. 7g) have collapsed and cracks extending from the pore walls into the matrix can be seen. Fig. 7h is imaged on the failed internal surface of the sample without further preparation. Similar to Fig. 7g, the black arrows indicate the positions of the collapsed pores, whereas the region within the dotted rectangular shape shows relatively rough cleavage bands. Surface roughening may be attributed to the microstructural change on the failed surface of the sample. The presence of the cleavage bands suggests that the failure of the pore walls and matrix is a blend of shear and brittle failures due to the limited slip systems in the hexagonal close-pack crystal structure of Mg. Similar microstructural observations have been reported in the failure analyses of composites of bulk Mg [11,26] and Mg-based foams [29]. In summary, the major mechanisms describing the failure of the foam samples can be identified as crack initiation and propagation relatively parallel to the loading direction, and a mixed-mode of shear and brittle failures of the pore walls and matrix.

4. Conclusions

An efficient processing scheme, comprising powder metallurgy, rapid microwave sintering, and matrix reinforcement has been successfully utilised to fabricate magnesium alloy AZ61 composite foams with enhanced compressive and energy absorption properties. Spherical carbamide granules are used to control the porosity, pore distribution, size, and shape in the foam samples. The experimental results indicate that the mixing technique utilised in this study is very effective in dispersing and incorporating CNTs into the matrix alloy without loss of structural integrity. Moreover, due to the synergism between the internal CNTs and external SiC/graphite susceptors, microwave sintering is very rapid and is completed in 20 minutes. The behaviours of the samples are similar under compression loading and test results show significant improvements in the compressive strength and energy absorption properties of CNT-reinforced composite

foams, in comparison with those of the unreinforced foams. The major mechanisms responsible for the failure of the foam samples are the initiation of cracks and their propagation along the loading direction, as well as a mixed mode of shear and brittle failure of the pore walls and matrix. The processing scheme proposed in this study can minimise the formation of brittle interfacial products and reduce the processing time and production cost, without releasing toxic gases, in the fabrication of lightweight magnesium alloy composite foams with enhanced mechanical properties.

Acknowledgments

The work described in this study was fully supported by the Hong Kong PhD Fellowship Scheme (HKPFS) of the Research Grants Council, RGC, The Government of the Hong Kong Special Administrative Region (Project Code: 1-904Z).

References

[1] G.A. Lara-Rodriguez, I.A. Figueroa, M.A. Suarez, O. Novelo-Peralta, I. Alfonso, R. Goodall, A replication-casting device for manufacturing open-cell Mg foams, J. Mater. Process. Technol. 243 (2017) 16–22. doi:10.1016/j.jmatprotec.2016.11.041.

[2] J. Čapek, D. Vojtěch, Properties of porous magnesium prepared by powder metallurgy, Mater. Sci. Eng. C. 33 (2013) 564–569. doi:10.1016/j.msec.2012.10.002.

[3] I. Duarte, M. Vesenjak, L. Krstulović-Opara, Variation of quasi-static and dynamic compressive properties in a single aluminium foam block, Mater. Sci. Eng. A. 616 (2014) 171–182. doi:10.1016/j.msea.2014.08.002.

[4] M.F. Ashby, A.G. Evans, N.A. Fleck, L.J. Gibson, J.W. Hutchinson, H.N.G. Wadley, Metal foams: a design guide, Butterworth-Heinemann, Boston, US, 2000.

[5] D.H. Yang, B.Y. Hur, S.R. Yang, Study on fabrication and foaming mechanism of Mg foam using CaCO3 as blowing agent, J. Alloys Compd. 461 (2008) 221–227. doi:10.1016/j.jallcom.2007.07.098.

[6] B.J.C. Luthringer, N. Hort, F. Feyerabend, Metal matrix composites: magnesium, Wiley Encycl. Compos. (2012) 1–23.

[7] M. Garcia-Avila, M. Portanova, A. Rabiei, Ballistic performance of composite metal foams, Compos. Struct. 125 (2015) 202–211. doi:10.1016/j.compstruct.2015.01.031.

[8] N. Bekoz, E. Oktay, Effects of carbamide shape and content on processing and properties of steel foams, J. Mater. Process. Tech. 212 (2012) 2109–2116. doi:10.1016/j.jmatprotec.2012.05.015.

[9] E. Aghion, T. Yered, Y. Perez, Y. Gueta, The prospects of carrying and releasing drugs via biodegradable magnesium foam, Adv. Eng. Mater. 12 (2010) B374–B379. doi:10.1002/adem.200980044.

[10] Y. Bi, Y. Zheng, Y. Li, Microstructure and mechanical properties of sintered porous magnesium using polymethyl methacrylate as the space holder, Mater. Lett. 161 (2015) 583–586. doi:10.1016/j.matlet.2015.09.039.

[11] A.D. Akinwekomi, W.-C. Law, C.-Y. Tang, L. Chen, C.-P. Tsui, Rapid microwave sintering of carbon nanotube-filled AZ61 magnesium alloy composites, Compos. Part B Eng. 93 (2016) 302–309. doi:10.1016/j.compositesb.2016.03.041.

[12] M.-T. Choy, C.-Y. Tang, L. Chen, W.-C. Law, C.-P. Tsui, W.W. Lu, Microwave assisted-in situ synthesis of porous titanium/calcium phosphate composites and their in vitro apatite-forming capability, Compos. Part B Eng. 83 (2015) 50–57. doi:10.1016/j.compositesb.2015.08.046.

[13] F.-P. Du, E.-Z. Ye, W. Yang, T.-H. Shen, C.-Y. Tang, X.-L. Xie, X.-P. Zhou, W.-C. Law, Electroactive shape memory polymer based on optimized multi-walled carbon nanotubes/polyvinyl alcohol nanocomposites, Compos. Part B Eng. 68 (2015) 170–175. doi:10.1016/J.COMPOSITESB.2014.08.043.

[14] T.Y. Zhou, G.C.P. Tsui, J.Z. Liang, S.Y. Zou, C.Y. Tang, V. Mišković-Stanković, Thermal properties and thermal stability of PP/MWCNT composites, Compos. Part B Eng. 90 (2016) 107–114. doi:10.1016/J.COMPOSITESB.2015.12.013.

[15] L. Chen, J.X. Wang, C.Y. Tang, D.Z. Chen, W.C. Law, Shape memory effect of thermal-responsive nano-hydroxyapatite reinforced poly-d-l-lactide composites with porous structure, Compos. Part B Eng. 107 (2016) 67–74. doi:10.1016/J.COMPOSITESB.2016.09.046.

[16] K. Kondoh, H. Fukuda, J. Umeda, H. Imai, B. Fugetsu, M. Endo, Microstructural and

mechanical analysis of carbon nanotube reinforced magnesium alloy powder composites, Mater. Sci. Eng. A. 527 (2010) 4103–4108. doi:10.1016/j.msea.2010.03.049.

[17] I. Duarte, E. Ventura, S. Olhero, J.M. Ferreira, A novel approach to prepare aluminium-alloy foams reinforced by carbon-nanotubes, Mater. Lett. 160 (2015) 162–166. doi:10.1016/j.matlet.2015.07.115.

[18] Y. Wu, G.Y. Kim, Carbon nanotube reinforced aluminum composite fabricated by semi-solid powder processing, J. Mater. Process. Technol. 211 (2011) 1341–1347. doi:10.1016/j.jmatprotec.2011.03.007.

[19] S. Simões, F. Viana, M.A.L. Reis, M.F. Vieira, Influence of dispersion/mixture time on mechanical properties of Al-CNTs nanocomposites, Compos. Struct. 126 (2015) 114–122. doi:10.1016/j.compstruct.2015.02.062.

[20] H.A. Mindivan, A.B. Efe, A.H.B. Kosatepe, E.S.C. Kayali, Fabrication and characterization of carbon nanotube reinforced magnesium matrix composites, Appl. Surf. Sci. 318 (2014) 234–243. doi:10.1016/j.apsusc.2014.04.127.

[21] Y. Shimizu, S. Miki, T. Soga, I. Itoh, H. Todoroki, T. Hosono, K. Sakaki, T. Hayashi, Y.A. Kim, M. Endo, S. Morimoto, A. Koide, Multi-walled carbon nanotube-reinforced magnesium alloy composites, Scr. Mater. 58 (2008) 267–270. doi:10.1016/j.scriptamat.2007.10.014.

[22] A. Agarwal, S.R. Bakshi, D. Lahiri, Carbon nanotubes : reinforced metal matrix composites, CRC Press, Boca Raton, 2010.

[23] J.A. Menéndez, A. Arenillas, B. Fidalgo, Y. Fernández, L. Zubizarreta, E.G. Calvo, J.M. Bermúdez, Microwave heating processes involving carbon materials, Fuel Process. Technol. 91 (2010) 1–8. doi:10.1016/j.fuproc.2009.08.021.

[24] C.E. Wen, Y. Yamada, K. Shimojima, Y. Chino, H. Hosokawa, M. Mabuchi, Compressibility of porous magnesium foam: dependency on porosity and pore size, Mater. Lett. 58 (2004) 357–360. doi:10.1016/S0167-577X(03)00500-7.

[25] G.L. Hao, F.S. Han, J. Wu, X.F. Wang, Mechanical and damping properties of porous AZ91 magnesium alloy, Powder Metall. 50 (2007) 127–131. doi:10.1179/174329007X153297.

[26] M.K. Habibi, M. Paramsothy, A.M.S. Hamouda, M. Gupta, Using integrated hybrid

(Al+CNT) reinforcement to simultaneously enhance strength and ductility of magnesium, Compos. Sci. Technol. 71 (2011) 734–741. doi:10.1016/j.compscitech.2011.01.021.

[27] D.-H. Yang, Y. Shang-Run, W. Hui, M. Ai-Bin, J. Jing-Hua, C. Jian-Qing, W. Ding-Lie, Compressive properties of cellular Mg foams fabricated by melt-foaming method, Mater. Sci. Eng. A. 527 (2010) 5405–5409. doi:10.1016/j.msea.2010.05.017.

[28] G.L. Hao, F.S. Han, W.D. Li, Processing and mechanical properties of magnesium foams, J. Porous Mater. 16 (2009) 251–256. doi:10.1007/s10934-008-9194-y.

[29] P. Li, N.V. Nguyen, H. Hao, Dynamic compressive behaviour of Mg foams manufactured by the direct foaming process, Mater. Des. 89 (2016) 636–641. doi:10.1016/j.matdes.2015.10.021.

[30] Y. Luo, S. Yu, W. Li, J. Liu, M. Wei, Compressive behavior of SiCp/AlSi9Mg composite foams, J. Alloys Compd. 460 (2008) 294–298. doi:10.1016/j.jallcom.2007.06.041.

[31] A. Esawi, K. Morsi, Dispersion of carbon nanotubes (CNTs) in aluminum powder, Compos. Part A Appl. Sci. Manuf. 38 (2007) 646–650. doi:10.1016/j.compositesa.2006.04.006.

[32] Z.Y. Liu, S.J. Xu, B.L. Xiao, P. Xue, W.G. Wang, Z.Y. Ma, Effect of ball-milling time on mechanical properties of carbon nanotubes reinforced aluminum matrix composites, Compos. Part A Appl. Sci. Manuf. 43 (2012) 2161–2168. doi:10.1016/j.compositesa.2012.07.026.

[33] H.J. Choi, J.H. Shin, D.H. Bae, The effect of milling conditions on microstructures and mechanical properties of Al/MWCNT composites, Compos. Part A Appl. Sci. Manuf. 43 (2012) 1061–1072. doi:10.1016/j.compositesa.2012.02.008.

[34] S. Sankaranarayanan, Q.B. Nguyen, R. Shabadi, A.H. Almajid, M. Gupta, Powder metallurgy hollow fly ash cenospheres' particles reinforced magnesium composites, Powder Metall. 59 (2016) 188–196. doi:10.1080/00325899.2016.1139339.

[35] H. Cay, H. Xu, Q. Li, Mechanical behavior of porous magnesium/alumina composites with high strength and low density, Mater. Sci. Eng. A. 574 (2013) 137–142. doi:10.1016/j.msea.2013.03.012.

[36] R. Surace, L.A.C. De Filippis, A.D. Ludovico, G. Boghetich, Influence of processing parameters on aluminium foam produced by space holder technique, Mater. Des. 30

(2009) 1878–1885. doi:10.1016/j.matdes.2008.09.027.

[37] R. Goodall, A. Mortensen, Porous metals, in: D.E. Laughlin, K. Hono (Eds.), Phys. Metall., Fifth Edit, Elsevier B.V., 2014: pp. 2399–2595. doi:10.1016/B978-0-444-53770-6.00024-1.

[38] Z. Zhang, J. Ding, X. Xia, X. Sun, K. Song, W. Zhao, B. Liao, Fabrication and characterization of closed-cell aluminum foams with different contents of multi-walled carbon nanotubes, Mater. Des. 88 (2015) 359–365. doi:10.1016/j.matdes.2015.09.017.

[39] S. Shima, M. Oyane, Plasticity theory for porous metals, Int. J. Mech. Sci. 18 (1976) 285–291.

Figure Captions

Fig. 1. FESEM micrographs of (a) entangled mass of as-received CNTs; (b) homogeneous distribution of CNTs on AZ61 powder after surfactant treatment (AZ61/3vol% CNT); (c) CNTs embedded on AZ61 surface after milling for 30 minutes (AZ61/3vol% CNT) (d) after milling for 60 minutes (AZ61/3vol% CNT); (e) agglomerates of CNTs in AZ61/5vol% CNT; and (f) persistent agglomerates of CNTs after milling (e) for 60 minutes.

Fig. 2. Raman spectra of (a) as-received CNTs and (b) AZ61/3vol% CNT milled for 60 minutes.

Fig. 3. XRD patterns of (a) AZ61 powder, (b) sintered AZ61 foam, (c) sintered AZ61/1vol% CNT foam (d) sintered AZ61/2vol% CNT foam and (e) AZ61/3vol% CNT foam. Foam porosity is 49%.

Fig. 4. Reconstructed 3D micro-CT images of AZ61 foams (a) 62% porosity (b) 49% porosity and longitudinal 2D slices through the foam samples (c) 62% porosity (d) 49% porosity.

Fig. 5. Compressive stress-strain curves of samples with (a) 48% porosity and (b) 62% porosity.

Fig. 6. Variation of yield stress with density for sintered AZ61 samples.

Fig. 7. (a) Typical stress-strain curve of a representative foam sample with 49% porosity; (b) to (f) Images of the different stages of failure of the sample under uniaxial compression as indicated by the arrows in (a); (g) SEM image of the internal microstructure of a failed surface sectioned parallel to the loading direction; and (h) SEM image of the shear bands on a failed surface.

Tables

Table 1 Raman spectra of as-received CNTs and AZ61/3% CNTs milled for 60 minutes.

Table 2 Comparison of the porosity, density, pore diameter and compressive characteristics of porous AZ61/CNTs composite foams and metallic foams.

Table 3 Estimation of energy saving in microwave sintering of magnesium-based composite foams.

Table 4 Comparison of experimental with calculated yield stresses.